Curvature-based pebble segmentation for reconstructed surface meshes

Aljoscha Rheinwalt[1], Benjamin Purinton[1], and Bodo Bookhagen[1]

[1]Institute of Geosciences, University of Potsdam, Karl-Liebknecht-Str. 24-25, Potsdam-Golm 14476, Germany

Correspondence: Aljoscha Rheinwalt (aljoscha.rheinwalt@uni-potsdam.de)

Abstract. Accurate segmentation of pebbles in complex 3D scenes is essential to understand sediment transport and river dynamics. In this study, we present a curvature-based instance segmentation approach for detecting and characterizing pebbles from 3D surface reconstructions. Our method is validated using high-resolution ground truth models, allowing for a quantitative assessment of segmentation accuracy. The workflow involves reconstructing a sandbox scene using available open-source or commercial software packages, segmenting individual pebbles based on curvature features, and evaluating segmentation performance using detection metrics, primary axes estimation, 3D orientation retrieval, and surface area comparisons. Results show a high detection precision (0.980), with segmentation errors primarily attributed to under-segmentation caused by overly smooth surface reconstructions. Primary axis estimation via bounding box fitting proves more reliable than ellipsoid fitting, particularly for the A and B axes, while the C-axis remains the most challenging due to partial occlusion. 3D orientation estimation reveals variability, with cumulative errors ranging from less than 5° to more than 45°, highlighting the difficulty in retrieving full orientations from incomplete segments. Surface area metrics indicate that our approach prioritizes precision over recall, with nine out of ten ground truth pebbles achieving IoU values above 0.8. In addition, we introduce a Python-based segmentation tool that provides detailed morphological and color-based metrics for each detected pebble. Our findings emphasize the advantages of true 3D analysis over traditional 2D photo-sieving approaches and suggest future improvements through refined segmentation algorithms and enhanced surface reconstructions.

1 Introduction

The characteristics of eroded material on hillslopes, river channels, and sedimentary deposits inform us about the physical, biological, and chemical mechanisms of sedimentary transport. Tectonic, climatic, hydrologic, and geomorphic driving forces generate a given size and shape distribution. By studying these distributions in time and space, we can gain insight into universal processes across different scales (e.g., Domokos et al., 2015, 2020; Szabó et al., 2015; Novák-Szabó et al., 2018). In particular, there is great interest in the size and shape distribution of pebbles in gravel-bed rivers, which can unravel downstream fining processes (e.g., Paola et al., 1992; Ferguson et al., 1996; Domokos et al., 2014; Miller et al., 2014; Lamb and Venditti, 2016), help us manage resources (e.g., Kondolf and Wolman, 1993; Kondolf, 1997; Grant, 2012), and calibrate transport and erosion models (e.g., Sklar et al., 2006; Attal and Lavé, 2006).

25   Accurate empirical measurements are paramount when studying pebbles. In traditional grain sieving, a sample of the local population is passed through progressively finer meshes, and the weight of the sample left behind on each mesh is measured. Then, the relative weight of each mesh-determined size class is converted into a percentage of that size. Considering the pebbles as approximating ellipsoids, this size is defined by the long a-axis or intermediate b-axis, and conversion factors from square mesh holes are used to retrieve axes parameters (Bunte and Abt, 2001). The main alternative to sieving is manual measurement

30   with rulers or calipers (e.g., Wolman, 1954; Wohl et al., 1996). Manual measurement with calipers provides a continuous distribution of grain sizes, but requires subjective determination of axis length in the field by an operator, and is generally a time-intensive process leading to small sample sizes. Particle templates are sometimes used instead of calipers, which can increase speed, but again, lead to binned measurements (Bunte and Abt, 2001).

    Recently, (semi-) automated image segmentation (e.g., Detert and Weitbrecht, 2012; Buscombe, 2013; Purinton and Bookha-

35   gen, 2019), sometimes referred to as "photo-sieving" (Ibbeken and Schleyer, 1986), has become a popular alternative to manual measurement. For 2D image segmentation methods (as opposed to image texture methods; cf. Purinton and Bookhagen, 2019), it is typical to use the ellipse model to retrieve a- and b-axes (e.g., Graham et al., 2005). These methods can lead to much larger sample sizes in far less time than manual measurement (e.g., Purinton and Bookhagen, 2021), but this is complicated by partially buried material, lighting, irregular pebble shapes, and image quality, all leading to high uncertainties (Graham et al.,

40   2010; Purinton and Bookhagen, 2021; Chardon et al., 2022; Mair et al., 2022). Many recent studies have also explored the utility of machine learning (convolutional neural networks) for measuring pebbles on 2D imagery (Buscombe, 2020; Soloy et al., 2020; Takechi et al., 2021; Lang et al., 2021; Chen et al., 2022; Mair et al., 2024), but these techniques require significant calibration and training data, and their universal applicability is yet to be determined. Of great concern, we note that any pebble shape determination on a 2D projected plane will likely suffer from an additional bias introduced by tilting the pebble, such

45   that the c-axis is not pointing directly upwards (cf. Fig. 2).

    Pebble shapes are determined from simple a-, b-, and c-axis ratios (Krumbein, 1941), descriptors like "platy", "bladed", or "elongated" (cf. Bunte and Abt, 2001), and equations based on axis measurements (e.g., sphericity $= (b \cdot c/a^2)^{1/3}$; Bunte and Abt, 2001). Such metrics are, however, based on the ellipsoid model, which reduces the entire shape of the pebble to three-axis measurements and may be prone to uncertainty caused by subjective manual measurements or 2D projection bias of the tilted

50   grain. The ellipsoid model does not take advantage of the full, irregular pebble surface. Some authors have expanded on axis measurements to look at roundness and curvature of the pebble surface, but often measured in a 2D image projection (e.g., Durian et al., 2007; Roussillon et al., 2009; Miller et al., 2014; Cassel et al., 2018), and less frequently from a 3D model (Hayakawa and Oguchi, 2005; Domokos et al., 2014). The proliferation of point-cloud data in geosciences, spurred by the widespread adoption of low-cost structure-from-motion with multi-view stereo (SfM-MVS; Smith et al., 2015) processing of

55   photographs, has ushered in a new age of 3D environmental analysis (Eltner et al., 2016). Whereas lidar point clouds may be expensive and/or time-consuming to collect and require co-registration of different views, point clouds from SfM-MVS can be quickly gathered with a consumer-grade camera and provide a full 3D view of the object from all sides without the need for point-cloud co-registration. However, the accuracy of SfM-derived point-clouds depends on several parameters, including image quality, image direction and orientation, number of images, and image contrast (Smith et al., 2015; Carrivick et al.,
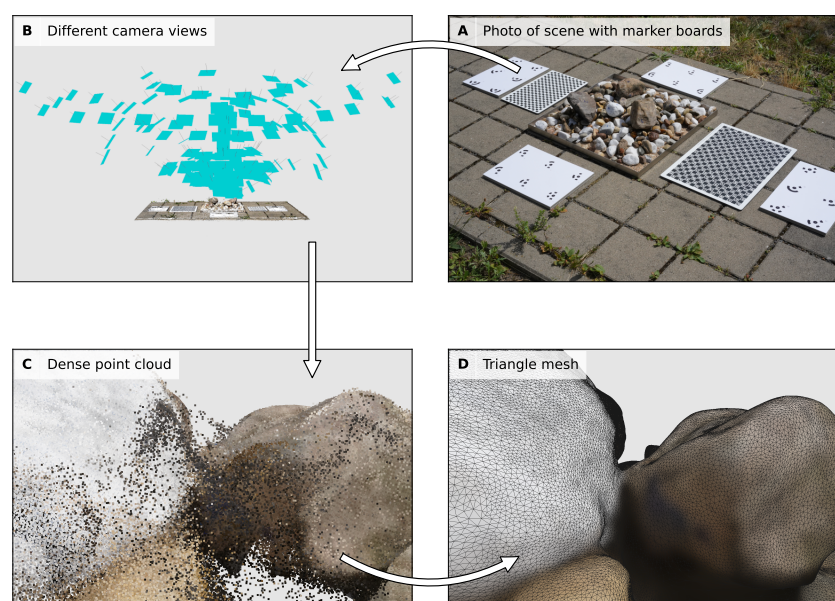
Figure 1. Reconstructed high-resolution triangle mesh as a 3D pebble model using Structure-from-Motion (SfM). (A) Overview photo of the entire scene that is also used in the SfM reconstruction. (B) Visualization of all camera views used. (C) Resulting high-resolution unfiltered dense point cloud, and (D) the corresponding triangle mesh zoomed to detail individual triangles.

60 2016). An assessment of SfM point-cloud accuracy for mm-scale pebble measurements has not been conducted but is required to assess measurement-related uncertainties.

Point clouds, and triangle mesh surfaces derived from them, allow accurate axis measurements by avoiding 2D projection biases, and allow measurement of additional 3D parameters in addition to axis lengths, like volume and surface area, which cannot be calculated in 2D. We note that *mesh* herein refers to the point-cloud derived product and not the mesh contained

65 in sediment sieves (Fig. 1). In fluvial grain-size measurement, volumetric, or volume-by-weight, sampling refers to the act of selecting samples of pebbles from different layers of the riverbed (surface and sub-surface) in a predefined volume of each layer, and then measuring the size distribution in the given volume of sediment by sieving, manual measurement, or image analysis. This use of volume is distinct from our definition of the volume of an individual grain, as could be measured by displacing water or from a point-cloud derived mesh.

70 Point clouds have already been used to measure grain size on riverbeds, but primarily via their texture, or roughness, which can be related to average grain size rather than a full distribution (e.g., Brasington et al., 2012; Rychkov et al., 2012; Westoby et al., 2015). An exciting prospect is the segmentation of individual grains from a point cloud, allowing for a full 3D model of every visible pebble down to a measurement limit determined by the point-cloud resolution (and thus image resolution in the
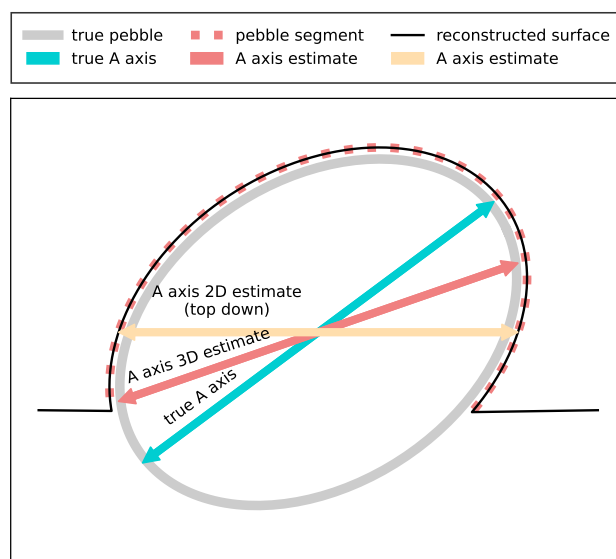
Figure 2. Schematic highlighting the differences between 2D and 3D A-axis estimates and the true A-axis length. By design, a 2D estimate will underestimate the axis length as soon as the true axis is tilted. However, a 3D estimate can underestimate the axis length if crucial parts of the pebble are hidden or not well reconstructed.

case of SfM-MVS). Walicka and Pfeifer (2022) presented a method based on random forest classification and then clustering to
75   segment grains, and Steer et al. (2022) presented another network-based method that segments the point cloud into watersheds to obtain grain boundaries. These methods provide reasonable segmentation results, although both have several parameters that must be set, and the performance remains qualitative.

    We are motivated by these developments to present another approach and algorithm for point-cloud segmentation for grain-size analysis based on 3D triangle meshes. A mesh is a network structure consisting of nodes (vertices), edges, and faces
80   (triangles). The nodes are the XYZ point positions, and the edges connect these to form the faces. A mesh can turn an unstructured point cloud into a structured network. Meshes contain more detailed information about the surface of an object than point clouds because they express the relationships between points. Meshes are an inherent output product of SfM processing and provide a convenient data structure for high-resolution surface calculation. Because of the neighborhood structure of meshes, there is no need to identify neighboring points, e.g., through a k-nearest neighbor query.

85 ## 2   Material and Methods

2.1   Material

For our experiments, we used a 0.5m × 0.5m stainless steel sandbox filled with fine sand obtained from a hardware store. To facilitate accurate scaling and alignment of the reconstructed 3D models, we placed calibration chess boards and custom-made

	1	2	3	4	5	6	7	8	9	10
Number of vertices:	1.1 M	2.0 M	4.0 M	3.8 M	2.2 M	0.8 M	0.6 M	1.1 M	0.5 M	0.4 M
Average triangle area:	0.003 mm²	0.009 mm²	0.005 mm²	0.004 mm²	0.003 mm²	0.003 mm²	0.004 mm²	0.003 mm²	0.005 mm²	0.003 mm²
Main axis length:	A: 56 mm	A: 147 mm	A: 143 mm	A: 113 mm	A: 69 mm	A: 55 mm	A: 42 mm	A: 53 mm	A: 50 mm	A: 39 mm
	B: 47 mm	B: 108 mm	B: 98 mm	B: 96 mm	B: 67 mm	B: 48 mm	B: 38 mm	B: 35 mm	B: 37 mm	B: 32 mm
	C: 25 mm	C: 79 mm	C: 94 mm	C: 65 mm	C: 50 mm	C: 29 mm	C: 27 mm	C: 36 mm	C: 31 mm	C: 12 mm
Volume:	35 ml	474 ml	580 ml	380 ml	103 ml	31 ml	24 ml	35 ml	24 ml	7 ml
Sphericity:	0.86	0.83	0.93	0.93	0.94	0.87	0.96	0.92	0.91	0.76
A/B axis ratio:	1.21	1.36	1.45	1.18	1.02	1.14	1.12	1.50	1.34	1.21

Figure 3. Overview of ten individual reference pebbles shown in a top-down view together with various characteristics of their corresponding 3D model. Those models serve as ground truth and are globally matched into the full 3D scene with all remaining pebbles and sand.

boards designed with special markers for automatic detection by Agisoft Metashape (cf. Fig. 1). For validation purposes, we included ten numbered pebbles alongside additional unnumbered pebbles to create a realistic scene (Fig. 3).

In a separate setup, to validate the accuracy of our 3D surface reconstruction, we created a structured formation by stacking colored table tennis balls inside the sandbox. These spheres provide an ideal test case for evaluating the geometric fidelity of the reconstructed surface, as their known size and smooth curvature allow for precise error analysis (cf. Fig. 5 and 6).

The final setup consisted of a fully populated sandbox scene containing 318 pebbles, including the ten numbered pebbles. This scene represents a realistic and complex test case for evaluating our segmentation approach under natural occlusions and varying pebble arrangements. The surface reconstruction and segmentation results from this setup form the core of our analysis.

2.2 3D scene reconstruction

Since we propose to count, measure, and characterize river pebbles in virtual reality, we need to retrieve 3D reconstructions of real scenes. This is convenient with modern open source Structure-for-Motion (SfM) software such as OpenMVG/OpenMVS (Cernea, 2020) or commercial software such as Agisoft Metashape Professional (AgiSoft PhotoScan Standard, Version 2.1.2, retrieved from http://www.agisoft.com/downloads/installer/). The software processes a set of photos from a scene of interest by performing a bundle adjustment to estimate camera parameters and positions, with a following multi-view stereo depth-map generation to retrieve a dense RGB-colored point cloud of the scene. This point cloud can also be converted to a triangle mesh, which is more useful because it provides an explicit surface. Our segmentation approach requires a triangle mesh that can be generated directly from SfM software or calculated from an existing point cloud using surface reconstruction techniques such as Poisson surface reconstruction (Kazhdan et al., 2006). The latter requires point clouds with normals and, in our experience, these meshes are never as accurate as those retrieved directly from OpenMVS or Agisoft Metashape.

Although modern digital cameras capture photos of unprecedented detail, 3D scene reconstructions will never be perfect. For segmenting and measuring pebbles, it is important to know how accurate a reconstruction is, what parameters influence
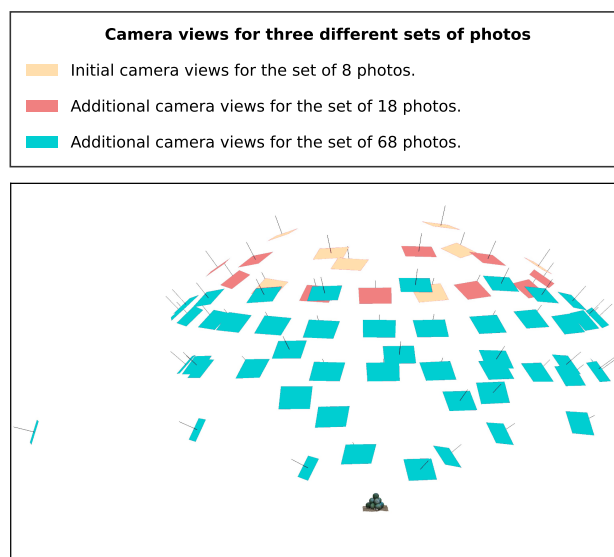
Figure 4. Visualization of the 68 different camera views for the table tennis validation setup. Photos are grouped into three sets for the analysis of reconstruction accuracies. Although top-down views are crucial, additional more oblique views can increase the reconstruction accuracy tremendously (cf. Fig. 5 and 6).

110   the quality, and how. For a control on that, we prepared a $0.5\,\text{m}$ x $0.5\,\text{m}$ steel sandbox with sand, gravel, and table tennis balls. In total, we took 68 photos of that sandbox from various angles around the scene (cf. Fig. 4). From this set of photos, we made three separate reconstructions. One with only eight of the most top-down view photos (cf. Fig. 5A), another with 18 of the most top-down view photos (cf. Fig. 5B), and a third with all 68 photos (cf. Fig. 5C). We apply our segmentation routine for all three reconstructions and generate a single triangle mesh for each table tennis ball. Since table-tennis balls are manufactured as

115   spheres with a radius of exactly $20\,\text{mm}$, the geometry is precisely known, and we can compare segments from reconstructions. We compare by fitting a model of a sphere to each triangle mesh segment, which provides us with a radius for every vertex of that mesh segment. We calculate a distribution of radii for each reconstructed table tennis ball (cf. Fig. 5). The more narrow and centered the distribution is around the true radius of $20\,\text{mm}$, the better.

As expected, reconstructions are more accurate if more photos from different angles are used. This is reflected in a more

120   accurate confirmation of table tennis ball radii with more photos. For the maximum of 68 photos, all radius distributions are more or less centered around $20\,\text{mm}$ and well confined between $20.0 \pm 0.5\,\text{mm}$. The accuracy can also be quantified by the root-mean-square-error (RMSE) of table tennis ball radii. With 8 photos from near-nadir positions a single table tennis ball has an RMSE of above 1 mm; for 68 photos all table tennis ball radii are well confined with an RMSE of below $0.4\,\text{mm}$ (cf. Fig. 6).

Overall, this makes photogrammetry a viable option for 3D surface reconstruction of river pebbles if the density of photos

125   matches the required accuracy. In our segmentation application scene of the same sandbox filled with sand and pebbles, we use
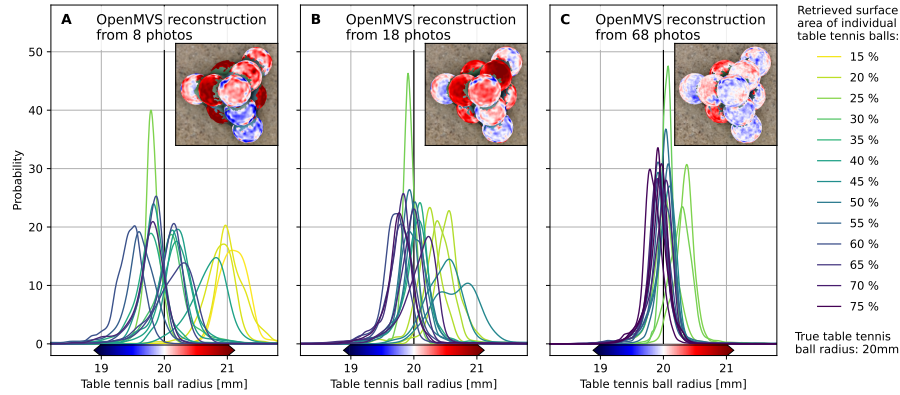
Figure 5. Reconstruction accuracy calculated for the number of photos used. Results for 8 (A), 18 (B), and 68 photos (C) from a real scene with 17 table tennis balls with radius 20 mm. All are individually segmented using our approach, and mesh vertices of a segment are used to fit the model of a sphere. In other words, we are fitting a spherical model to each mesh triangle identified for the segmented table tennis ball. Depending on the residuals of this model, each vertex corresponds to a slightly different radius, leading to a distribution of radii for each segment. These radius distributions are shown in shades of yellow to blue depending on the retrieved surface area of the true, full table tennis ball. The most complex part of the scene is a stack of 10 table tennis balls, shown in insets. Here, segments are colored according to radius residuals. The more photos used, the smaller the residuals, and the more narrow and centered around the true radius of 20 mm the radius distributions get. For 68 photos, most radii are well constrained within the interval of 20.0 ± 0.5 mm, constituting an uncertainty of about 2.5%.

157 photos for 3D surface reconstruction. Hence, we can expect an even more accurate surface reconstruction compared to the table tennis experiment.

In addition to reconstructing the entire sandbox scene containing sand and river pebbles, we also generated separate high-resolution 3D models for ten marked and numbered pebbles from the scene. Each of these pebble models was independently reconstructed using a dedicated set of photos captured under controlled conditions. For this process, the pebbles were placed against a white background and rotated to ensure full coverage. Each dataset consisted of 66 to 158 photographs taken from very short distances, resulting in very high-resolution triangle mesh models with average triangle areas ranging between 0.003 mm^2 and 0.009 mm^2 (cf. Fig.3).

The individual pebble models exhibit a diverse range of sizes and shapes, with some containing approximately half a million vertices and others reaching up to 4 million vertices (Fig.3). This variety ensures a broad representation of geometries, enhancing their utility as benchmarks. The primary purpose of these detailed pebble models is to align them with the reconstructed sandbox scene and compare retrieved pebble segments to these high-resolution models, which serve as ground truth. This allows us to evaluate the segmentation algorithm's accuracy in identifying and reconstructing individual pebbles within the scene.
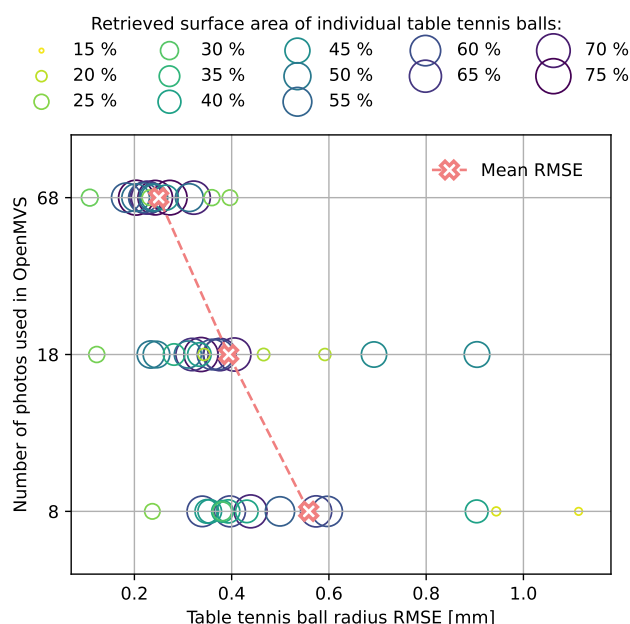
Figure 6. From the same experiment of Fig. 5 the reconstruction accuracy is shown in terms of root mean square errors (RMSE) of model residuals. Each segment is represented by a circle in shades of yellow to blue. The color and size indicate the retrieved surface area of the segment. Better-represented segments tend to be closer to the mean RMSE. The latter is going down with an increase in photos used, but generally, the RMSE goes towards zero. For the best case of 68 photos, the RMSE is below $0.4\,\text{mm}$ for all segments.

Additionally, these high-resolution models provide an independent means of validating the overall scene reconstruction. By comparing the integrated, lower-resolution pebble representations within the scene to their corresponding high-resolution counterparts, we can further assess the fidelity of the reconstruction process. This dual-purpose approach strengthens the reliability of the reconstructed sandbox scene while offering robust ground truth data for testing segmentation accuracy.

2.3 Curvature based segmentation

Our curvature-based mesh segmentation algorithm offers an efficient approach to identifying and isolating convex parts within a 3D mesh. The process begins by computing the mean curvature for each triangle in the mesh, distinguishing between concave (cf. green parts in Fig. 7B), convex (purple parts in Fig. 7B), and flat regions (white parts in Fig. 7B). Triangles with concave curvatures are discarded, leaving only those with convex or zero curvature. The retained regions are grouped into connected components (cf. colored parts in Fig. 7C) and refined through post-processing steps, such as topological hole filling to ensure continuity and erosion to eliminate thin bridges that might otherwise connect distinct pebbles. Finally, the components are filtered based on their sphericity, removing predominantly flat segments. This ensures that the resulting segments consist of convex regions that may include flat areas but maintain an overall curved structure. These pre-processing and filtering steps make the algorithm ideal for isolating meaningful convex features in complex geometric data (cf. colored segments in Fig. 7D).
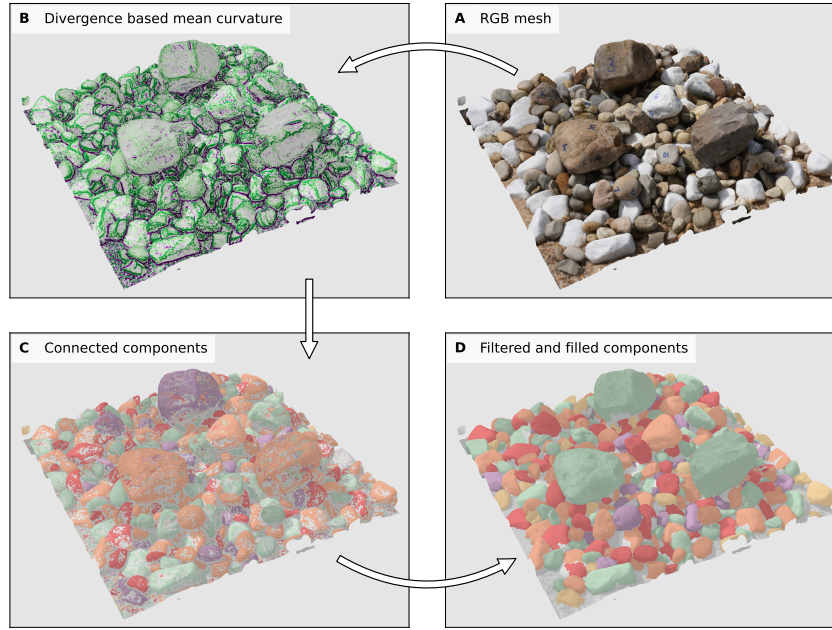
Figure 7. Workflow pipeline for the $0.5\,\mathrm{m} \times 0.5\,\mathrm{m}$ test sandbox filled with sand and pebbles, including the ten numbered archetypical pebbles (cf. Fig. 3). First, a 3D triangle mesh is reconstructed from RGB photos (A). RGB information is only used for visualization. Second, the mean curvature is computed from the divergence of mesh vertex normals (B). Third, all concave parts (purple) of the mesh are removed, and the remaining parts (green and white) are labeled as connected components (C). Fourth, the components are filtered based on size and sphericity, as well as topologically filled to retrieve the final pebble segments (D).

At the core of our segmentation algorithm is an accurate and robust method for estimating mean curvature, which is derived
155   from the divergence of the normal field (Eq.1). Conceptually, the divergence of surface normals provides a clear distinction between surface types: diverging normals indicate convex regions, while converging normals correspond to concave surfaces. Mathematically, mean curvature H relates to surface normals $\boldsymbol{n}$ in 3D in the following way:

$$2H = -\nabla \cdot \boldsymbol{n} \,. \tag{1}$$

Our normal field, though inherently defined only on the mesh surface, is extended into the surrounding 3D space using
160   inverse distance interpolation. The divergence at a point is computed as:

$$\nabla \cdot \boldsymbol{n} = \frac{\partial n_x}{\partial x} + \frac{\partial n_y}{\partial y} + \frac{\partial n_z}{\partial z} \,, \tag{2}$$

where $\boldsymbol{n}$ represents the interpolated normal field. For each triangle, the normal field around its center is calculated using inverse distance weighting from nearby vertex normals. The partial derivatives are estimated using finite differences, requiring offset positions along the x, y, and z axes. The offsets are automatically determined as twice the mean distance to the 25 nearest

165   neighbors of the triangle, ensuring local adaptivity. Results are robust to changes in the number of 25 neighbors. If the number is much larger, it will introduce a smoothing of the curvature field. Generally, this number should be as small as possible while still retaining good statistics for the offset as the mean distance. This extension of the surface normal field into 3D enables a precise computation of the divergence, which serves as the basis for determining mean curvature and distinguishing concave, convex, and flat regions.

170   In our segmentation algorithm, post-processing steps such as hole filling, erosion, and dilation are implemented directly for triangle meshes, drawing inspiration from well-established concepts in mathematical morphology and image analysis. While these techniques are widely available for image-based data, we are unaware of software providing equivalent functionality for triangle meshes, prompting us to develop our own implementation. Here, triangles play the role of pixels, enabling these operations to be adapted to 3D geometry.

175   For hole filling, instead of permanently discarding triangles with concave curvature, we initially mark them for potential removal. During post-processing, holes are detected topologically by identifying connected components among the concave triangles. If a set of concave triangles is found to be touching only a single convex segment, it is classified as a hole in that segment and merged back with it. This ensures that holes within otherwise convex regions are accurately filled.

   Erosion is performed by iteratively removing triangles from a segment if they are adjacent to other triangles already marked
180 for removal. This approach allows for the progressive thinning of segments by peeling away layers of triangles. Dilation, the reverse process, adds triangles back to a segment if they are adjacent to the segment and were previously marked for removal. This optional step helps mitigate over-shrinking caused by erosion while ensuring that new additions do not connect previously distinct segments. These operations, tailored specifically to triangle meshes, enable precise refinement of convex segments while preserving their structural integrity and topological boundaries. For a very high-quality mesh with clear and not
185 smoothed-out curvatures between pebbles, erosion and dilation would not be required because pebbles would be well separated by concave curvatures.

   We provide the Python source code and Jupyter Notebook guides in a GitHub repository that explains pre-processing and filtering steps with multiple examples.

2.4   Validation Using High-Resolution Ground Truth Models

190 To validate the quality of our proposed pebble segmentation approach, we leverage the high-resolution ground truth models of ten marked pebbles, which were independently reconstructed with significantly higher fidelity. After the segmentation of the real scene, we align these ground truth models with the reconstructed sandbox scene using the Fast-Point-Feature-Histogram-based fast global registration method (Rusu et al., 2009; Zhou et al., 2016). This alignment ensures accurate positioning of the high-resolution pebble models within the reconstructed scene, providing a reliable basis for comparison.

195   Once aligned, we evaluate the segmentation approach using several metrics derived from the retrieved pebble segments in the scene and their corresponding ground truth models. These metrics focus on both geometric and structural aspects, ensuring a comprehensive assessment:

Pebble Dimensions (A, B, and C axes): The primary axes of each pebble, denoted as A (longest), B (intermediate), and C (shortest), are extracted from both the segmented pebbles and the ground truth models. The comparison of these axes provides insights into the accuracy of the shape and size representation in the segmentation process.

3D Orientation (Yaw, Pitch, and Roll): The orientation of each pebble is evaluated using the yaw, pitch, and roll angles. These angles describe the rotation of the pebbles in 3D space and are compared between the segmented pebbles and their ground truth counterparts to assess alignment accuracy.

Surface Area Metrics (Intersection over Union, Precision, and Recall): To evaluate how well the segmented pebble surfaces correspond to the ground truth, we compute the Intersection over Union (IoU), which measures the overlap between the retrieved surface area of a segmented pebble and its ground truth model. Additionally, precision and recall are calculated to quantify the accuracy and completeness of the retrieved surface area. Precision reflects the proportion of correctly identified pebble surfaces within the segmentation, while recall indicates the proportion of the ground truth surface correctly captured in the segmentation.

For the validation of pebble dimensions, we focus on the primary axes, A (longest), B (intermediate), and C (shortest). As a first step, the A axes of the real pebbles were measured using calipers prior to their inclusion in the sandbox. These measurements were used to scale the corresponding high-resolution ground truth models, ensuring an accurate physical correspondence between the models and the real-world pebbles.

The other two axes, B and C, were estimated from the ground truth models by fitting a bounding box aligned to each model's internal datum or coordinate system (cf. Fig. 8). This coordinate system is derived from the pebble's geometry using principal component analysis (PCA), ensuring alignment to its primary axes. For consistency, the same bounding box approach was used to estimate the A, B, and C axes of the pebble segments from the reconstructed scene. The differences between the axes derived from the segmented pebbles and those of the scaled ground truth models were then calculated to evaluate the accuracy of the segmentation.

In addition to the bounding box method, we also estimated the primary axes of the pebble segments using ellipsoid fitting, a common technique in the literature for approximating pebble dimensions (e.g., Steer et al., 2022). This method involves fitting an ellipsoid to the segmented pebble and using its semi-principal axes as proxies for the A, B, and C axes (cf. Fig. 8). However, our results show that the bounding box method generally produces more accurate estimations with lower deviations from the ground truth.

While pebble orientations have not been widely studied, they hold potential for revealing important information about river flow dynamics, riverbank collapses, and pebble movements. Our primary objective in this validation is to assess whether pebble orientations can be accurately estimated from typically incomplete segments of pebbles within the reconstructed scene.

To evaluate orientation accuracy, we compare the internal datum of the high-resolution ground truth models with that of the corresponding pebble segments. The internal PCA-derived datum for each model and segment identifies the primary axes of the object and aligns them with a local coordinate system. This orientation of a local coordinate system (cf. Fig. 9) provides the basis for comparing yaw, pitch, and roll angles between the ground truth models and their segmented counterparts.
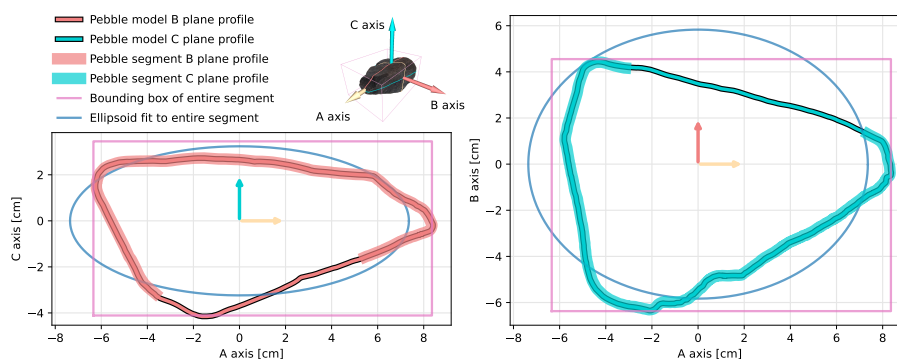
Figure 8. Illustration of the difference between the bounding box and ellipsoid-based main axis length estimation for the same pebble of Fig. 9. Shown are B-plane profiles on the left-hand side and C-plane profiles on the right-hand side for the segment from a reconstruction (incomplete profiles) as well as from the true model. Axis length estimations from bounding boxes are less prone to over- or underestimations when compared to ellipsoid estimations.
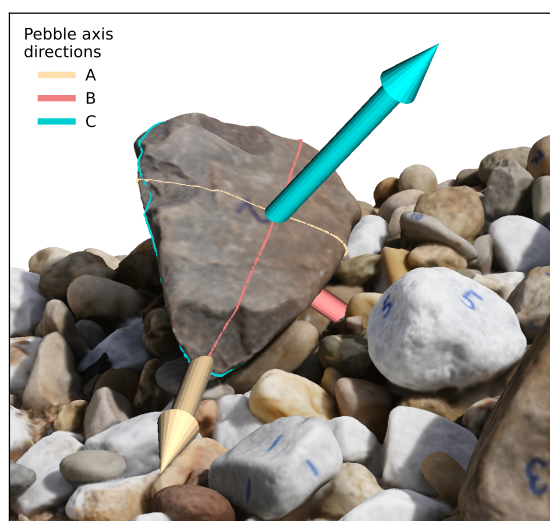
Figure 9. Illustration of pebble main axis directions and the internal datum of a pebble. Pebbles can be characterized by a xyz-position of the centroid as well as the orientation of its main axes in terms of three rotations: roll, pitch, and yaw.
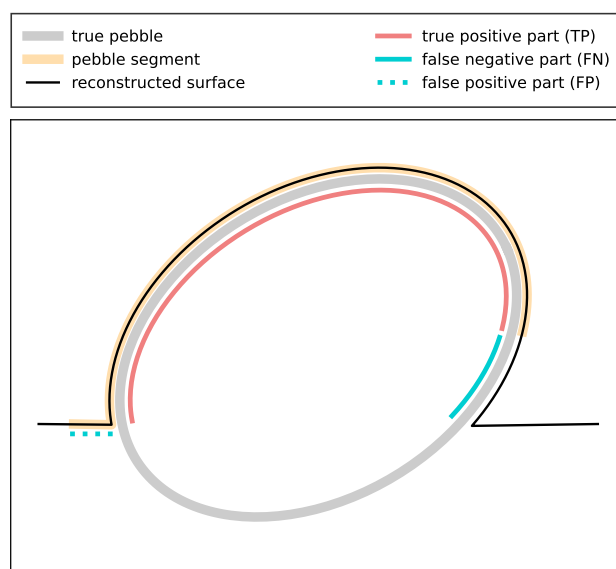
Figure 10. Schematic illustration of a pebble segment and its reconstructed surface area, highlighting the true positive region (TP), false negative region (FN), and false positive region (FP), from which precision, recall, and intersection over union (IoU) are calculated.

A key challenge in this comparison arises from the incomplete nature of the pebble segments in the real scene. Significant portions of the ground truth models are often occluded by other pebbles or sand in the reconstructed scene, which can lead to discrepancies between the two orientation estimates. Despite this, our results indicate that the orientation estimates are generally robust. The largest observed angular difference occurred for the yaw angle of pebble number five, with a deviation of 25° (see Results Section 3).

For the validation of our segmentation approach using surface area metrics, we also leverage the high-resolution ground truth models of the pebbles. These models contain complete surface information, including portions of the pebbles that are not retrievable from the reconstructed scene, as they may be hidden behind other pebbles or buried in sand. Consequently, our segmentation approach can only recover the visible portion of each pebble present in the scene.

To address this limitation, we first determine the retrievable part of each ground truth model by applying a distance threshold of two millimeters. This threshold identifies the triangles in the scene's mesh that are within two millimeters of the surface of a ground truth model. The resulting region represents the best-case segment – the portion of the ground truth model that is theoretically recoverable from the scene. This best-case segment serves as the reference for evaluating the segmentation.

For comparison, we overlay the best-case segment with the corresponding segmented region obtained from our algorithm. Each triangle in the scene is then categorized as one of the following: True Positive (TP), a triangle that belongs to both the segmented region and the best-case segment. False Positive (FP) is a triangle that belongs to the segmented region but not to the best-case segment. False Negative (FN) is a triangle that belongs to the best-case segment but is missing from the segmented region (cf. Fig. 10).

250 Using these classifications, we compute the total true positive, false positive, and false negative surface areas. From these, we derive the following metrics:

$$\text{Precision} = \frac{TP}{TP + FP} \tag{3}$$

$$\text{Recall} = \frac{TP}{TP + FN} \tag{4}$$

$$\text{IoU} = \frac{TP}{TP + FP + FN} \tag{5}$$

255 This evaluation framework ensures that the performance of our segmentation approach is rigorously assessed in terms of its ability to accurately recover the retrievable portion of each pebble. By comparing these metrics across multiple pebbles, we can quantify both the strengths and limitations of the segmentation algorithm and identify areas for potential improvement.

2.5 Camera and Photo Capture

We have used several cameras and lenses to generate reconstructions. In general, the various reconstructions from different
260 cameras performed equally well, and we provide some general suggestions for photo-shooting.

We used a Sony alpha6000 (ILCE-6000 v3.20) with 24 MP (6000x4000 pixels) and a fixed 35 mm lens (Sony E 35mm F1.8) to generate reconstructions of the individual 10 pebbles. We used the same camera for the reconstruction of the table tennis scene. We used a Sony alpha7III (ILCE-7RM3) with 42.2 MP (7952x5304 pixels) with a fixed lens (Sony FE 35mm F1.8) for the sandbox pebble scene. Although the Sony Alpha7III has a larger number of pixels, we did not observe relevant
265 quality differences between the 24MP and 42MP reconstructions because the images were taken from close range. However, we observe differences in point densities in far-field photography.

We manually measured the a-axis of the ten numbered pebbles with a caliper and scaled the individual pebble reconstructions accordingly. For the reconstruction of the table tennis scene and the pebble sandbox scene, we used several marker boards as a scale (cf. Fig. 1). We created A4-sized boards with 6 numbered markers that can be automatically detected by software. The
270 distances of the markers were 12 cm in the x and y directions. We used four boards, one on each side, with a total of 24 markers to scale and orient photos. In addition to markers used by Agisoft Metashape, we used camera calibration boards by calib.io to scale reconstruction within OpenMVS and perform camera calibration experiments. We note the benefit of multiple marker boards in the scene to guide photo alignment during the SfM process and to expedite camera optimization routines.

We did not perform a separate camera calibration but experimented with various approaches. Camera calibration may be
275 useful and necessary for scenes with lower photo numbers and overlap. Since our reconstructions were based on very dense and highly overlapping photos, the boundary conditions for camera optimization procedures were well defined. In addition, the fixed lenses we have used provide high-quality images, and the optical distortion does not vary with time. The camera optimization steps based on SIFT features generally provide good camera parameter estimations for close-range photos.

We have used additional cameras to reconstruct scenes with similar results (not shown). We would like to de-emphasize
280 the importance of a specific camera to reconstruct scenes and instead make some general observations to improve scene reconstructions. A full-format sensor with a fixed lens will provide excellent results. A fixed lens is necessary to ensure that

camera optics remain comparable between acquisitions. We suggest avoiding zoom lenses. We suggest turning off all automatic correction parameters. Modern cameras tend to have a large number of correction schemes that may help an individual photo but are not beneficial during bundle adjustment. In particular, we turn off distortion and color corrections, noise and exposure corrections, autofocus tracking, and other intelligent default settings common to modern digital cameras.

2.6 3D Surface Reconstruction with OpenMVG and OpenMVS

For the 3D surface reconstruction of our sandbox scene and individual pebbles, we employed an incremental structure-from-motion (SfM) and multiview stereo (MVS) pipeline using the open source software OpenMVG and OpenMVS. This workflow enabled the generation of dense point clouds and reconstructed meshes from input images. In the following, we outline the key steps and commands used in the reconstruction process.

Structure-from-Motion with OpenMVG The incremental SfM pipeline in OpenMVG was used to compute camera poses and a sparse point cloud:

```
# Step 1: Initialize the scene
openMVG_main_SfMInit_ImageListing -i images -o output -d sensor_width_database.txt

# Step 2: Compute features
openMVG_main_ComputeFeatures -i output/sfm_data.json -o output

# Step 3: Compute matches
openMVG_main_ComputeMatches -i output/sfm_data.json -o output

# Step 4: Incremental reconstruction
openMVG_main_IncrementalSfM -i output/sfm_data.json -m output -o output

# Step 5: Convert to OpenMVS format
openMVG_main_ConvertSfM_DataFormat -i output/sfm_data.bin -o output/scene.mvs -o2
```

Multi-View Stereo with OpenMVS After obtaining the camera poses and sparse point cloud from OpenMVG, we performed dense reconstruction and meshing using OpenMVS:

```
# Step 6: Densify the point cloud
DensifyPointCloud -i output/scene.mvs -o output/scene_dense.mvs

# Step 7: Generate the mesh
ReconstructMesh -i output/scene_dense.mvs -o output/scene_mesh.ply
```

This workflow allowed us to obtain high-resolution 3D models of both the entire sandbox scene and individual pebbles. The
incremental SfM pipeline in OpenMVG ensured robust camera pose estimation, while OpenMVS provided high-quality dense
reconstructions and meshes from the computed sparse point cloud.

2.7 3D Surface Reconstruction with Metashape

The quality of the output point clouds of Agisoft Metashape and OpenMVS are largely comparable, and we do not intend
to provide a quality comparison. Instead, we only present an alternative approach using familiar, paid software. We note that
the triangle meshes produced by OpenMVS have higher resolution, i.e., more and smaller triangles, and are therefore used
throughout this study. However, for the case of many photos taken from a short distance, the differences are not important for
the segmentation.

We rely on Agisoft Methashape (Version 2.1.2) to align, bundle adjust, and generate dense point clouds. After photo import,
we detect markers and add scale bars. Automatic marker detection allows for faster alignment of photos without accurate GNSS
photo tags. We filter detected SIFT features (called tie points in Metashape) and remove unreliable matches. We use projection
error, reconstruction uncertainty, and projection accuracy to iteratively remove tie points with large covariances and generate a
homogeneous covariance distribution. Bundle adjustment (camera optimization) is performed after each tie-point removal step.
We calculate depth maps (or dense point clouds) only after sufficient filtering of the tie points. We emphasize the importance
of a clean tie-point dataset before proceeding to the depth map generation. The accuracy of the point cloud largely depends on
an accurate estimation of camera positions, which is achieved during the bundle adjustment step.

Agisoft Metashape allows the generation of meshes directly from depth maps, and we suggest to directly export meshes
(e.g., as ply files) for further processing. However, the mesh generation within Metashape performs smoothing and filtering
steps to reduce the number of vertices. It may be required to customize the number of vertices that you aim for. If you decide
to use point clouds, we suggest exporting points with normals to speed up the mesh generation step via Poisson reconstruction.

3 Results

Our segmentation approach provides four main results, which we evaluate using various metrics and comparisons.

3.1 Detection of Pebbles in the Scene

The first result concerns the detection accuracy of all pebbles in the reconstructed sandbox scene. A pebble is considered
successfully detected (true positive) if it is represented by a distinct segment. False positives occur due to over-segmentation
(cf. Fig. 11), where a single pebble is represented by multiple segments, while false negatives arise from small pebbles being
missed or multiple pebbles being grouped into a single segment (under-segmentation).

In our reconstructed scene, which contains 318 visible pebbles:

- True detection positives: 297
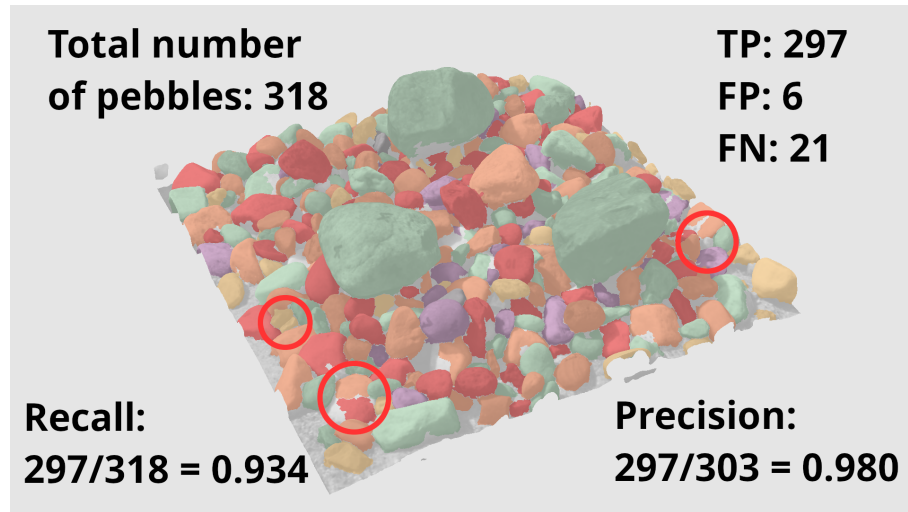
Figure 11. From this specific example scene of 318 pebbles, 297 were correctly identified (true positives, TP), i.e., 21 pebbles were missed (false negatives, FN). However, due to over-segmentation, 6 additional false pebbles were detected (false positives, FP). This gives us a precision of 0.980, a recall of 0.934, and an intersection over union (IoU) of 0.917.

    – False detection positives: 6

345   – False detection negatives: 21

From these counts, we calculate the following metrics for detection performance:

Detection precision: $\frac{297}{297+6} = 0.980$

Detection recall: $\frac{297}{297+21} = 0.934$

Detection Intersection over Union (IoU): $\frac{297}{297+21+6} = 0.917$

350   These results demonstrate the effectiveness of the segmentation approach, with high precision indicating a low rate of over-segmentation and strong recall highlighting the ability to identify most pebbles in the scene.

3.2   Estimation of Primary Axes for Ground Truth Pebbles

The second result focuses on the estimation of the primary axes (A, B, and C) for the ten pebbles in the scene that correspond to our ground truth models. We compare two methods for estimating these axes: the bounding box method and ellipsoid fitting

355   (cf. Fig. 12).

When analyzing the cumulative axes errors (sum of A, B, and C errors) across the ten pebbles:

Bounding box method: Eight out of ten pebbles had lower cumulative errors compared to the ellipsoid fitting method.
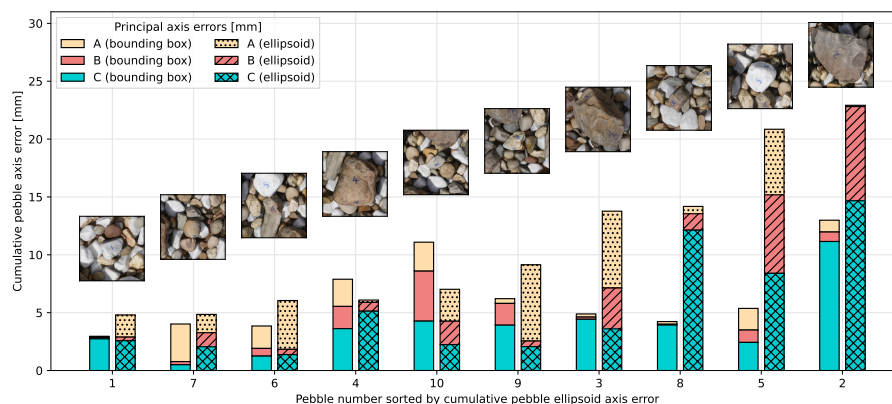
Figure 12. Comparison of ellipsoid and bounding box derived principal axis errors. For ten archetypical pebbles, full 3D models were matched into the scan of a real scene also containing these pebbles. After segmentation and principal axis estimation from bounding boxes or ellipsoid fits, segment axes are compared to their true full 3D model axes. Axis estimations from bounding boxes are most often more accurate than those retrieved from ellipsoid fits.

Ellipsoid fitting method: Only two out of ten pebbles showed smaller cumulative errors using this method.

Specific observations:

- The smallest cumulative error was well below $0.5\,\text{cm}$ and was achieved using the bounding box method for pebble no. 1.

- The largest cumulative error occurred with ellipsoid fitting for pebble no. 2 and was larger than $2\,\text{cm}$.

- Across both methods, errors were dominated by inaccuracies in estimating the C axis (shortest axis), indicating a consistent challenge in resolving this dimension.

These results confirm that the bounding box method provides more accurate and reliable axis estimations than ellipsoid fitting, particularly for pebbles with complex or irregular shapes.

3.3 Estimation of 3D Orientations

The third result evaluates the accuracy of 3D orientation estimations (yaw, pitch, and roll angles) for the ten ground truth pebbles in the scene (cf. Fig.13 for an example). Orientation errors are highly variable across the pebbles, with cumulative angle errors ranging from below 5° to above 45° (cf. Fig. 14):

- The smallest cumulative error ($< 5°$) was observed for pebble no. 7.

- The largest cumulative error ($> 45°$) occurred for pebble no. 5.

- Five pebbles had cumulative angle errors of 20° or less, while the remaining five exhibited larger errors.
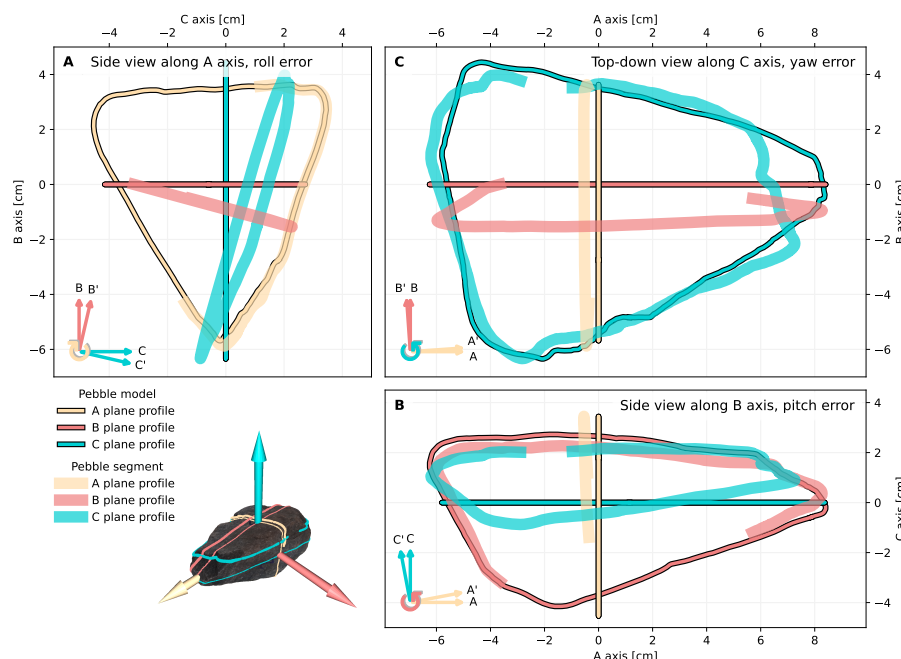
Figure 13. Orientation errors for pebble number two as an example. Orientations retrieved from segments are generally different from orientations of full 3D models. We define orientation in terms of yaw, pitch, and roll angles, and differences in these as orientation errors. The roll error is visible in the side view along the A axis (A), the pitch error in the side view along the B axis (B), and the yaw error in the top-down view along the C axis (C). The less a pebble is exposed, the greater the orientation error. In other words: As pebble exposure decreases, orientation errors increase. (cf. Fig. 14).

Interestingly, there appears to be no clear relationship between pebble size and orientation errors. Instead, the variability in errors is likely influenced by pebble shape, geometry, and possibly by surface area recall (see the fourth result). Despite the challenges posed by incomplete segments in the scene, the orientation estimations for some pebbles, such as no. 7, were remarkably accurate.

3.4 Surface Area Metrics

The fourth result focuses on our surface area metrics precision, recall, and Intersection over Union (IoU) for the ten ground truth pebbles. Overall, the results are highly encouraging (cf. Fig. 15):

- For nine out of the ten pebbles, precision, recall, and IoU values exceeded 0.8.

- Pebble no. 2, which had the lowest IoU, still achieved a very high precision value (close to 1), although its recall was above 0.75.
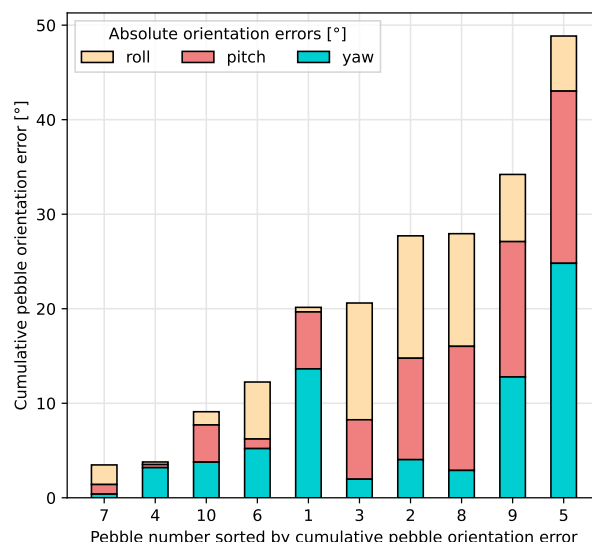
Figure 14. Cumulative absolute pebble orientation errors for the ten numbered pebbles. While cumulative errors reach almost 50°, orientations of individual axes are always below 30°, which is about 17% of the maximum error of 180°.
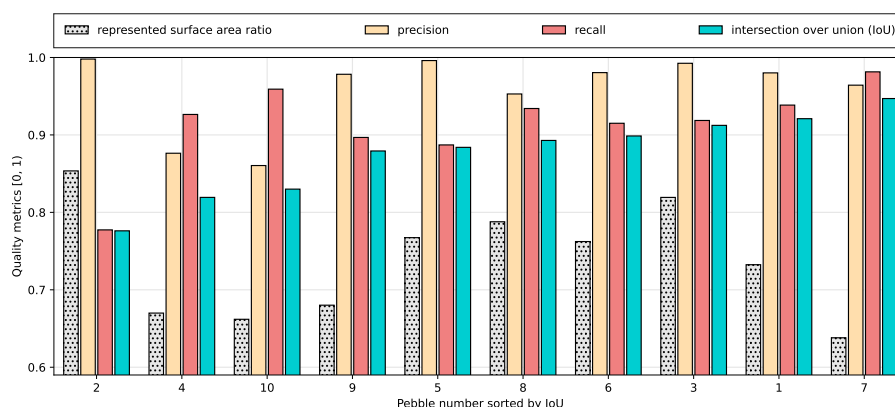
Figure 15. Segmentation quality in terms of precision, recall, and IoU of the segmented surface area versus the represented surface area. Not all pebbles are represented equally; some have a higher represented surface area than others. Although pebble number two has the best-represented surface area ratio, it has the worst recall and IoU. On the other hand, pebble seven has the worst represented surface-area ratio but the best recall and IoU.

- IoU values are ordered from lowest to highest (cf. Fig. 15), with pebble no. 2 having the lowest IoU and pebble no. 7 achieving an IoU close to 0.95.

385   A notable observation is that our segmentation approach tends to optimize precision over recall, as the majority of pebbles exhibit higher precision values. However, for pebbles no. 7, 4, and 10, recall values are higher than precision. Interestingly,

these three pebbles also have the smallest cumulative orientation errors, suggesting a possible link between accurately recalling segments and correctly estimating orientations.

In addition, we computed the represented surface area ratio, which measures the proportion of the full ground truth pebble that is present in the scene mesh. This ratio was lowest for the same three pebbles (no. 7, 4, and 10) that showed the smallest cumulative orientation errors. This suggests that it may be more critical for a segment to accurately recall the part of a pebble represented in the scene mesh rather than for the pebble to have a high surface area ratio in the reconstructed scene.

4 Discussion

Our proposed curvature-based mesh segmentation algorithm, combined with validation using high-resolution ground truth models, demonstrates strong potential for accurately segmenting and characterizing pebbles in complex 3D scenes. This discussion highlights key insights derived from this analysis, explores challenges, and considers implications for future applications and research.

4.1 Detection Performance

The segmentation approach achieved high detection accuracy, with a precision of 0.980, recall of 0.934, and IoU of 0.917 for the detection of 318 visible pebbles in the reconstructed sandbox scene. These metrics indicate that the algorithm effectively minimizes false positives caused by over-segmentation and false negatives caused by under-segmentation or missed pebbles. Notably, the number of false positives (6) is significantly lower than the number of false negatives (21). False positives are mostly due to over-segmentation, where a single pebble is incorrectly split into multiple segments. In contrast, false negatives arise from under-segmentation or missed detections, often caused by small pebbles being overlooked or multiple pebbles being merged into a single segment.

Both types of errors are influenced by the quality of the surface reconstruction. A highly smoothed mesh of the scene leads to washed-out features, making it difficult for the segmentation approach to identify boundaries between pebbles or the boundary around a small pebble. The worse the quality of the reconstructed surface, the smoother the curvatures become, resulting in reduced segmentation performance. Addressing this limitation may require enhancing the surface reconstruction process to preserve finer geometric details.

We emphasize the need for a high-quality mesh to accurately segment pebbles. The mesh quality is mostly related to the distance the photos are taken and their direction. While UAV-based acquisition with low flight height and near-nadir camera perspective will result in good orthomosaics, the 3D segmentation approach will require oblique views to capture the vertical component of pebbles. An alternative to UAV-based acquisition are mast-mounted cameras in 2 to 4 m heights (Purinton and Bookhagen, 2021). The camera quality on masts is often higher than the optical equipment used on UAVs, and a UAV flight height of a few meters above ground level poses threats to the data-acquisition team and bystanders and hazards to the UAV in difficult flight conditions.

4.2 Primary Axes Estimation

The bounding box method outperformed ellipsoid fitting for estimating primary axes in eight out of ten cases, demonstrating
420   its robustness, particularly for irregular pebble shapes. The dominance of C-axis errors in the cumulative errors underscores
the challenge of accurately estimating this axis, which is often the shortest and most affected by incomplete segmentation. This
difficulty arises because pebbles typically rest flat in the scene, meaning their bottom portions are often obscured by sand or
other pebbles. Consequently, the mesh of the scene usually only represents the top and sides of pebbles, making it harder to
estimate the shortest axis.

425   Despite these challenges, our approach provides true 3D estimations of the A and B axes, unlike common photo sieving
methods that rely on 2D projections onto the image plane. Such methods consistently underestimate A and B axes due to their
inability to capture the full 3D geometry of the pebbles. This limitation highlights the advantages of our bounding box method,
which accounts for the true spatial dimensions of the pebbles.

4.3 3D Orientation Estimation

430   Estimating 3D orientations (yaw, pitch, and roll) remains a challenging task, especially when segments are incomplete due
to occlusions or burial in sand. The variability in orientation errors across pebbles, ranging from less than 5° to more than
45°, reflects the sensitivity of principal component analysis (PCA)-based methods to incomplete surface data. Despite these
challenges, the strong correlation between high recall and accurate orientation estimation, as observed for pebbles no. 7, 4,
and 10, suggests that prioritizing recall during segmentation can improve orientation accuracy. This relationship merits further
435   exploration, particularly in the context of applications where pebble orientation is critical for understanding sediment dynamics.

In contrast to traditional methods based on orthomosaics or 2D projections, our approach retrieves true 3D orientations and
not just one orientation angle. For example, while yaw can sometimes be estimated from orthomosaics if the C-axis is perfectly
aligned with the nadir, any slight tipping of the C-axis leads to the underestimation of yaw. Pitch and roll are completely
unretrievable from 2D data. Our method, by leveraging the internal datum derived from PCA, ensures a more accurate and
440   comprehensive representation of pebble orientations in three dimensions.

4.4 Surface Area Metrics and Representation

The evaluation of surface area metrics such as precision, recall, and IoU, revealed that our segmentation approach tends to
optimize precision over recall. For nine out of ten pebbles, all three metrics exceeded 0.8, demonstrating the algorithm's
ability to capture retrievable segments with high fidelity. Notably, pebble no. 2, with the lowest IoU, still achieved near-perfect
445   precision, highlighting the segmentation algorithm's tendency to avoid under-segmentation at the expense of slightly lower
recall.

Interestingly, the three pebbles with recall greater than precision – pebbles no. 7, 4, and 10 – also had the smallest orientation
errors and lowest represented surface area ratios. This finding underscores the importance of ensuring that segments accurately

represent the portions of pebbles visible in the scene mesh. Future refinements could explore adaptive thresholds for balancing

450 precision and recall, potentially leading to improved performance across all metrics.

4.5   Example Application of the Segmentation Software

To illustrate the practical utility of our segmentation approach, we apply our Python software to the sandbox scene and demonstrate the resulting segmentation and quantitative analysis. The software performs instance segmentation and generates a table where each segmented pebble is assigned various attributes:

455 **Segment ID:** A unique identifier for each pebble.

Segment Color: A locally unique identifier useful for visualization, derived via graph coloring.

Centroid (X, Y, Z): Mean coordinates of the segment.

A, B, and C Axes: Derived using the bounding box method for efficiency and accuracy.

Yaw, Pitch, and Roll: Pebble orientation in degrees.

460 **Color Statistics:** Mean and standard deviation values for the red, green, and blue channels extracted from the mesh.

Surface Metrics: Segment surface area, convex hull surface area, convex hull volume, and convex hull sphericity.

Segment ID	0	1	2	3	4	...
Segment color	0	1	0	0	0	...
Centroid x [m]	0.055	0.083	-0.047	0.038	0.235	...
Centroid y [m]	-0.352	-0.312	-0.349	-0.200	-0.490	...
Centroid z [m]	0.042	0.073	0.039	0.078	0.032	...
A axis [m]	0.052	0.065	0.042	0.146	0.033	...
B axis [m]	0.050	0.068	0.031	0.108	0.028	...
C axis [m]	0.044	0.052	0.023	0.073	0.016	...
Yaw [°]	-171	88	-106	126	168	...
Pitch [°]	-5	4	-13	-14	-22	...
Roll [°]	-17	180	19	-19	-42	...
Red mean	0.497	0.656	0.366	0.358	0.452	...
Green mean	0.486	0.652	0.266	0.324	0.386	...
Blue mean	0.484	0.656	0.212	0.296	0.290	...
Red STD	0.239	0.216	0.139	0.177	0.196	...
Green STD	0.240	0.223	0.113	0.162	0.172	...
Blue STD	0.237	0.233	0.100	0.156	0.139	...
Mesh surface area [m^2]	0.00215	0.00856	0.00203	0.02484	0.00121	...
Convex hull area [m^2]	0.00582	0.01135	0.00312	0.03427	0.00195	...
Convex hull volume [10^{-5} m^3]	3.19	10.41	1.38	45.37	0.62	...
Convex hull sphericity [m^2/m^2]	0.836	0.943	0.893	0.833	0.838	...

As an example analysis, we extract and visualize the distributions of A, B, and C axis lengths across the segmented pebbles (cf. Fig. 16). The resulting histograms highlight the variability in pebble sizes, providing insights into grain size distribution 465 within the scene. This example demonstrates the broader potential of our methodology, offering a detailed, automated way to extract and analyze pebble attributes from 3D reconstructions.

4.6 Implications and Future Directions

Our findings have several implications for riverine and sedimentological studies. The ability to accurately segment and characterize pebbles, including their primary axes and 3D orientations, provides valuable data for understanding river flow dynamics, 470 sediment transport, and depositional processes. Additionally, the use of high-resolution ground truth models as a validation tool ensures rigorous assessment of segmentation accuracy, setting a standard for future research in this domain.

However, challenges remain, particularly in handling highly irregular shapes, small pebbles, and occlusions. Integrating complementary data sources, such as RGB color or hyperspectral information, could enhance segmentation robustness. Further, refining the algorithm's component-based approach to segmentation could improve its ability to handle complex topologies in
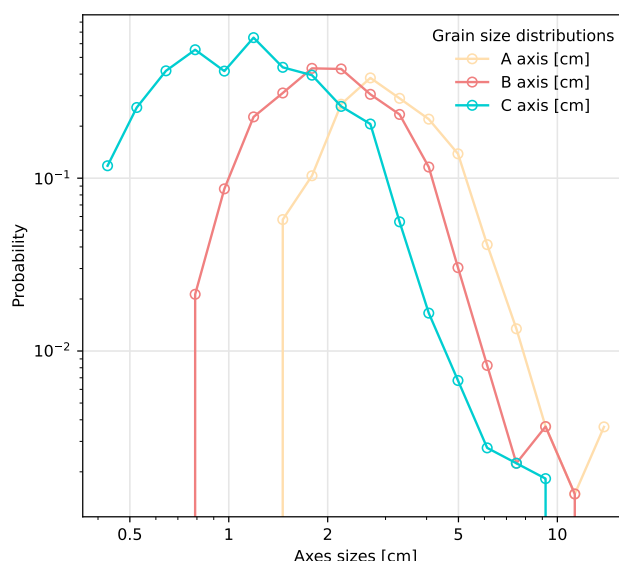
Figure 16. Example analysis of the sandbox scene and its corresponding grain size distributions for the A, B, and C axes lengths as computed by our Python software and available on github.

475 the mesh. In particular, more advanced techniques used in image segmentation approaches such as random walks will likely outperform our approach.

Finally, while our approach focuses on pebbles, its underlying principles are broadly applicable to other domains requiring curvature-based segmentation of 3D meshes, such as isosurfaces in medical imaging, size and orientation of speleothems in caves and karst, and trees in a forest. Future work could explore these applications, expanding the algorithm's impact beyond

480 sedimentology.

5 Conclusion

Precision of point cloud or triangle mesh surface reconstructions depends on the number of photos. With near-field photo acquisitions, we constrain uncertainties using table-tennis balls to an RMSE of below 2% in the ideal case of 68 photos. With only eight nadir photos, it is only below 6%.

485 We present a Python pipeline for our curvature-based mesh segmentation to delineate individual pebbles from a 3D scene. Our test field with 318 individual pebbles inside a 0.25 m^2 sandbox indicate a high detection accuracy, with segmentation errors primarily linked to under-segmentation due to overly smooth surface reconstructions. Bounding box-based primary axis estimation proves to be more reliable than an ellipsoidal fit for A and B axes, while C-axis estimation remains challenging due to occlusions. Surface area metrics highlight the trade-off between precision and recall, with our approach favoring precision.

490   True 3D pebble segmentation outperforms traditional 2D methods, providing a more complete representation of pebble orientations and primary axes, including the possibility of retrieving volumetric parameters.

We emphasize the need for a high-quality mesh that can be derived from multiple photo views from varying angles to successfully segment pebbles. Future work should focus on refining segmentation algorithms and improving surface reconstruction fidelity to enhance accuracy and applicability.

495   *Code availability.* The code used for pebble segmentation in this study is provided at https://doi.org/10.5281/zenodo.14987825 (Rheinwalt et al., 2025). This software is also maintained at https://github.com/UP-RS-ESP/mesh-curvature-instance-segmentation.

Data availability. Captured photos, from these photos reconstructed triangle mesh 3D models used in this study, as well as the Python software together with a tutorial can all be found at: https://doi.org/10.5281/zenodo.14987825 (Rheinwalt et al., 2025).

Author contributions. **Aljoscha Rheinwalt:** Conceptualization, Methodology, Software, Validation, Formal analysis, Visualization, Writing
500   - Original Draft. **Benjamin Purinton:** Methodology, Validation, Writing - Review & Editing. **Bodo Bookhagen:** Methodology, Validation, Writing - Review & Editing, Resources.

Competing interests. The authors declare no competing interests.

References

Attal, M. and Lavé, J.: Changes of bedload characteristics along the Marsyandi River (central Nepal): Implications for understanding hillslope

505   sediment supply, sediment load evolution along fluvial networks, and denudation in active orogenic belts, Geological Society of America
Special Papers, 398, 143–171, https://doi.org/10.1130/2006.2398(09), 2006.

Brasington, J., Vericat, D., and Rychkov, I.: Modeling river bed morphology, roughness, and surface sedimentology using high resolution
terrestrial laser scanning, Water Resources Research, 48, W11 519, https://doi.org/10.1029/2012WR012223, 2012.

Bunte, K. and Abt, S. T.: Sampling surface and subsurface particle-size distributions in wadable gravel- and cobble-bed streams for analyses

510   in sediment transport, hydraulics and streambed monitoring, Tech. rep., US Forest Service, Rocky Mountain Research Station, Fort Collins,
CO, https://doi.org/10.2737/RMRS-GTR-74, 2001.

Buscombe, D.: Transferable wavelet method for grain-size distribution from images of sediment surfaces and thin sections, and other natural
granular patterns, Sedimentology, 60, 1709–1732, https://doi.org/10.1111/sed.12049, 2013.

Buscombe, D.: SediNet: a configurable deep learning model for mixed qualitative and quantitative optical granulometry, Earth Surface

515   Processes and Landforms, 45, 638–651, https://doi.org/https://doi.org/10.1002/esp.4760, 2020.

Carrivick, J. L., Smith, M. W., and Quincey, D. J.: Background to Structure from Motion, chap. 3, pp. 37–59, John Wiley & Sons, Ltd,
https://doi.org/https://doi.org/10.1002/9781118895818.ch3, 2016.

Cassel, M., Piégay, H., Lavé, J., Vaudor, L., Hadmoko Sri, D., Wibiwo Budi, S., and Lavigne, F.: Evaluating a
2D image-based computerized approach for measuring riverine pebble roundness, Geomorphology, 311, 143–157,

520   https://doi.org/https://doi.org/10.1016/j.geomorph.2018.03.020, 2018.

Cernea, D.: OpenMVS: Multi-View Stereo Reconstruction Library, https://cdcseacave.github.io/openMVS, unpublished, 2020.

Chardon, V., Piasny, G., and Schmitt, L.: Comparison of software accuracy to estimate the bed grain size distribution from digital images:
A test performed along the Rhine River, River Research and Applications, 38, 358–367, https://doi.org/https://doi.org/10.1002/rra.3910,
2022.

525   Chen, X., Hassan, M. A., and Fu, X.: Convolutional neural networks for image-based sediment detection applied to a large terrestrial and
airborne dataset, Earth Surface Dynamics, 10, 349–366, https://doi.org/10.5194/esurf-10-349-2022, 2022.

Detert, M. and Weitbrecht, V.: Automatic object detection to analyze the geometry of gravel grains–a free stand-alone tool, in: River flow
2012 : Proceedings of the international conference on fluvial hydraulics, San José, Costa Rica, September 5-7, 2012, pp. 595–600, Taylor
& Francis Group, London, 2012.

530   Domokos, G., Jerolmack, D. J., Sipos, A. Á., and Török, Á.: How river rocks round: resolving the shape-size paradox, PloS one, 9, e88 657,
2014.

Domokos, G., Kun, F., Sipos, A. A., and Szabó, T.: Universality of fragment shapes, Scientific reports, 5, 9147, 2015.

Domokos, G., Jerolmack, D. J., Kun, F., and Török, J.: Plato's cube and the natural geometry of fragmentation, Proceedings of the National
Academy of Sciences, 117, 18 178–18 185, https://doi.org/10.1073/pnas.2001037117, 2020.

535   Durian, D. J., Bideaud, H., Duringer, P., Schröder, A. P., and Marques, C. M.: Shape and erosion of pebbles, Phys. Rev. E, 75, 021 301,
https://doi.org/10.1103/PhysRevE.75.021301, 2007.

Eltner, A., Kaiser, A., Castillo, C., Rock, G., Neugirg, F., and Abellán, A.: Image-based surface reconstruction in geomorphometry – merits,
limits and developments, Earth Surface Dynamics, 4, 359–389, https://doi.org/10.5194/esurf-4-359-2016, 2016.

Ferguson, R., Hoey, T., Wathen, S., and Werritty, A.: Field evidence for rapid downstream fining of river gravels through selective transport, Geology, 24, 179–182, https://doi.org/10.1130/0091-7613(1996)024<0179:FEFRDF>2.3.CO;2, 1996.

Graham, D. J., Reid, I., and Rice, S. P.: Automated Sizing of Coarse-Grained Sediments: Image-Processing Procedures, Mathematical Geology, 37, 1–28, https://doi.org/10.1007/s11004-005-8745-x, 2005.

Graham, D. J., Rollet, A.-J., Piégay, H., and Rice, S. P.: Maximizing the accuracy of image-based surface sediment sampling techniques, Water Resources Research, 46, W02 508, https://doi.org/10.1029/2008WR006940, 2010.

Grant, G. E.: The Geomorphic Response of Gravel-Bed Rivers to Dams: Perspectives and Prospects, chap. 15, pp. 165–181, Wiley-Blackwell, https://doi.org/10.1002/9781119952497.ch15, 2012.

Hayakawa, Y. and Oguchi, T.: Evaluation of gravel sphericity and roundness based on surface-area measurement with a laser scanner, Computers & Geosciences, 31, 735–741, https://doi.org/https://doi.org/10.1016/j.cageo.2005.01.004, 2005.

Ibbeken, H. and Schleyer, R.: Photo-sieving: A method for grain-size analysis of coarse-grained, unconsolidated bedding surfaces, Earth Surface Processes and Landforms, 11, 59–77, https://doi.org/10.1002/esp.3290110108, 1986.

Kazhdan, M., Bolitho, M., and Hoppe, H.: Poisson surface reconstruction, in: Proceedings of the fourth Eurographics symposium on Geometry processing, vol. 7, 2006.

Kondolf, G. M.: PROFILE: hungry water: effects of dams and gravel mining on river channels, Environmental management, 21, 533–551, 1997.

Kondolf, G. M. and Wolman, M. G.: The sizes of salmonid spawning gravels, Water Resources Research, 29, 2275–2285, 1993.

Krumbein, W. C.: Measurement and geological significance of shape and roundness of sedimentary particles, Journal of Sedimentary Research, 11, 64–72, https://doi.org/10.1306/D42690F3-2B26-11D7-8648000102C1865D, 1941.

Lamb, M. P. and Venditti, J. G.: The grain size gap and abrupt gravel-sand transitions in rivers due to suspension fallout, Geophysical Research Letters, 43, 3777–3785, https://doi.org/10.1002/2016GL068713, 2016.

Lang, N., Irniger, A., Rozniak, A., Hunziker, R., Wegner, J. D., and Schindler, K.: GRAINet: mapping grain size distributions in river beds from UAV images with convolutional neural networks, Hydrology and Earth System Sciences, 25, 2567–2597, https://doi.org/10.5194/hess-25-2567-2021, 2021.

Mair, D., Do Prado, A. H., Garefalakis, P., Lechmann, A., Whittaker, A., and Schlunegger, F.: Grain size of fluvial gravel bars from close-range UAV imagery–uncertainty in segmentation-based data, Earth Surface Dynamics, 10, 953–973, 2022.

Mair, D., Witz, G., Do Prado, A. H., Garefalakis, P., and Schlunegger, F.: Automated detecting, segmenting and measuring of grains in images of fluvial sediments: The potential for large and precise data from specialist deep learning models and transfer learning, Earth Surface Processes and Landforms, 49, 1099–1116, 2024.

Miller, K. L., Szabó, T., Jerolmack, D. J., and Domokos, G.: Quantifying the significance of abrasion and selective transport for downstream fluvial grain size evolution, Journal of Geophysical Research: Earth Surface, 119, 2412–2429, https://doi.org/https://doi.org/10.1002/2014JF003156, 2014.

Novák-Szabó, T., Sipos, A. Á., Shaw, S., Bertoni, D., Pozzebon, A., Grottoli, E., Sarti, G., Ciavola, P., Domokos, G., and Jerolmack, D. J.: Universal characteristics of particle shape evolution by bed-load chipping, Science advances, 4, eaao4946, https://doi.org/10.1126/sciadv.aao4946, 2018.

Paola, C., Parker, G., Seal, R., Sinha, S. K., Southard, J. B., and Wilcock, P. R.: Downstream Fining by Selective Deposition in a Laboratory Flume, Science, 258, 1757–1760, https://doi.org/10.1126/science.258.5089.1757, 1992.

Purinton, B. and Bookhagen, B.: Introducing *PebbleCounts*: a grain-sizing tool for photo surveys of dynamic gravel-bed rivers, Earth Surface Dynamics, 7, 859–877, https://doi.org/10.5194/esurf-7-859-2019, 2019.

Purinton, B. and Bookhagen, B.: Tracking Downstream Variability in Large Grain-Size Distributions in the South-Central Andes, Journal of Geophysical Research: Earth Surface, 126, e2021JF006 260, https://doi.org/https://doi.org/10.1029/2021JF006260, e2021JF006260 2021JF006260, 2021.

Roussillon, T., Piégay, H., Sivignon, I., Tougne, L., and Lavigne, F.: Automatic computation of pebble roundness using digital imagery and discrete geometry, Computers & Geosciences, 35, 1992–2000, https://doi.org/https://doi.org/10.1016/j.cageo.2009.01.013, 2009.

Rusu, R. B., Blodow, N., and Beetz, M.: Fast Point Feature Histograms (FPFH) for 3D registration, in: 2009 IEEE International Conference on Robotics and Automation, pp. 3212–3217, https://doi.org/10.1109/ROBOT.2009.5152473, 2009.

Rychkov, I., Brasington, J., and Vericat, D.: Computational and methodological aspects of terrestrial surface analysis based on point clouds, Computers & Geosciences, 42, 64–70, https://doi.org/10.1016/j.cageo.2012.02.011, 2012.

Sklar, L. S., Dietrich, W. E., Foufoula-Georgiou, E., Lashermes, B., and Bellugi, D.: Do gravel bed river size distributions record channel network structure?, Water Resources Research, 42, W06D18, https://doi.org/10.1029/2006WR005035, 2006.

Smith, M., Carrivick, J., and Quincey, D.: Structure from motion photogrammetry in physical geography, Progress in Physical Geography: Earth and Environment, 40, 247–275, https://doi.org/10.1177/0309133315615805, 2015.

Soloy, A., Turki, I., Fournier, M., Costa, S., Peuziat, B., and Lecoq, N.: A Deep Learning-Based Method for Quantifying and Mapping the Grain Size on Pebble Beaches, Remote Sensing, 12, https://doi.org/10.3390/rs12213659, 2020.

Steer, P., Guerit, L., Lague, D., Crave, A., and Gourdon, A.: Size, shape and orientation matter: fast and automatic measurement of grain geometries from 3D point clouds, EGUsphere, 2022, 1–31, https://doi.org/10.5194/egusphere-2022-75, 2022.

Szabó, T., Domokos, G., Grotzinger, J. P., and Jerolmack, D. J.: Reconstructing the transport history of pebbles on Mars, Nature communications, 6, 1–7, https://doi.org/10.1038/ncomms9366, 2015.

Takechi, H., Aragaki, S., and Irie, M.: Differentiation of River Sediments Fractions in UAV Aerial Images by Convolution Neural Network, Remote Sensing, 13, https://doi.org/10.3390/rs13163188, 2021.

Walicka, A. and Pfeifer, N.: Automatic Segmentation of Individual Grains From a Terrestrial Laser Scanning Point Cloud of a Mountain River Bed, IEEE Journal of Selected Topics in Applied Earth Observations and Remote Sensing, 15, 1389–1410, https://doi.org/10.1109/JSTARS.2022.3141892, 2022.

Westoby, M. J., Dunning, S. A., Woodward, J., Hein, A. S., Marrero, S. M., Winter, K., and Sugden, D. E.: Sedimentological characterization of Antarctic moraines using UAVs and Structure-from-Motion photogrammetry, Journal of Glaciology, 61, 1088–1102, https://doi.org/10.3189/2015JoG15J086, 2015.

Wohl, E. E., Anthony, D. J., Madsen, S. W., and Thompson, D. M.: A comparison of surface sampling methods for coarse fluvial sediments, Water Resources Research, 32, 3219–3226, https://doi.org/10.1029/96WR01527, 1996.

Wolman, M. G.: A method of sampling coarse river-bed material, Eos, Transactions American Geophysical Union, 35, 951–956, https://doi.org/10.1029/TR035i006p00951, 1954.

Zhou, Q.-Y., Park, J., and Koltun, V.: Fast global registration, in: Computer Vision–ECCV 2016: 14th European Conference, Amsterdam, The Netherlands, October 11-14, 2016, Proceedings, Part II 14, pp. 766–782, Springer, 2016.